Analog Maximum Peak Power Tracking Techniques for Small Satellites

CRISTIAN TORRES
AUSIÀS GARRIGÓS, Senior Member, IEEE
JOSÉ M. BLANES
PABLO CASADO
DAVID MARROQUÍ
Miguel Hernández University of Elche, Elche, Spain

This work describes the implementation of three maximum peak power tracking methods devised for small satellites. The three methods are the analog oscillating maximum power point tracking, the analog global maximum peak power tracking, and the analog global maximum output power tracking. An interplanetary mission (Mars–Asteroid belt) with complex power–voltage solar array characteristics, including several local maximum power points, is considered to evaluate each peak power tracking technique. The three peak power tracking techniques have been integrated into an unregulated battery bus topology using synchronous buck converters as solar array regulators. High-reliability design is achieved using analog electronic parts with space-qualified counterparts. Each peak power tracking method has been optimized individually for the best performance and then compared with the others. The experimental validation suggests that the preferred method strongly depends on the expected power–voltage solar array characteristics and mission parameters.

Manuscript received 21 September 2022; revised 19 December 2022 and 16 March 2023; accepted 9 May 2023. Date of publication 15 May 2023; date of current version 11 October 2023.

DOI. No. 10.1109/TAES.2023.3275935

Refereeing of this contribution was handled by R. Meyer.

This work was supported in part by the Generalitat Valenciana and the European Social Fund through the Subvención Para la Contratación de Personal Investigador de Carácter Predoctoral under Grant ACIF2020/154 and in part by the European Union NextGenerationEU and the Generalitat Valenciana under Grant ASFAE/2022/21.

Authors' address: The authors are with the Industrial Electronics Research Group, Miguel Hernandez University of Elche, Elche 03202, Spain, E-mail: (c.torres@umh.es; augarsir@umh.es; jmblanes@umh.es; pablo.casado@alu.umh.es; dmarroqui@umh.es). *(Corresponding author: Cristian Torres.)*

NOMENCLATURE

Acronyms and Definitions

AGMOPT	Analog global maximum output power tracking.
AGMPPT	Analog global maximum peak power tracking.
AMPPT	Analog maximum power point tracking.
AU	Astronomical unit.
CCM	Continuous conduction mode.
CLK	Clock signal (used in different circuits).
D_{AGMOPT}	Duty cycle (AGMOPT method).
D_{AGMPPT}	Duty cycle (AGMPPT method).
dc–dc	direct current to direct current.
DSP	digital signal processors.
EOC	End of charge (referred to battery).
ESA	European Space Agency.
EPS	Electrical power system.
f_{AMPPT}	Frequency of the AMPPT method.
$\mathrm{fc}_{\mathrm{io}}$	Cutoff frequency of the output current filter (AGMOPT method).
$\mathrm{fc}_{\mathrm{vin}}$	DC–dc converter input voltage control loop crossover frequency.
FOCV	Fractional open-circuit voltage.
f_{sw}	DC–dc converter switching frequency.
GMPP	Global maximum power point.
I_{LEAK}	Leakage current of the voltage reference circuit (referred to AGMPPT and AGMOPT methods).
K_i	Current sampling attenuation factor (AMPPT method).
K_v	Voltage sampling attenuation factor (AMPPT method).
LEO	Low Earth orbit.
LPF	Low-pass filter.
MOPT	Maximum output power tracking.
MPP	Maximum power point.
MPPT	Maximum peak point tracking (also referred as PPT).
PPT	Peak power tracking.
OC	Open circuit.
PCB	Printed circuit board.
PSO	Particle swarm optimization.
PWM	Pulsewidth modulation.
SA	Solar array.
SAR	Solar array regulator.
SC	Short circuit.
S&H$_v$	Sample and hold circuit for voltage (AMPPT method).
S&H$_i$	Sample and hold circuit for current (AMPPT method).
T_{AGMOPT}	Period of the AGMOPT method ($t_{\mathrm{SCAN}} + t_{\mathrm{MPOT}}$).
T_{AGMPPT}	Period of the AGMPPT method ($t_{\mathrm{OFF}} + t_{\mathrm{MPPT}}$).
t_{MPPT}	Time interval in which the solar array regulator operates at the GMPP (AGMPPT method).

t_{MOPT}	Time interval in which the solar array regulator operates at the maximum output power (AGMOPT method).
t_{OFF}	Time interval in which the dc–dc converter is turned OFF (AGMPPT method).
t_{SCAN}	Time interval in which the dc–dc converter is operated in a current control mode with a varying reference (AGMOPT method).
t_{ramp}	Time interval in which the ramp used to perform the scanning process is active (AGMOPT method).
t_{rvin}	Rise time of the dc–dc converter input voltage control loop.
$V_{\mathrm{AGMOPTref}}$	MPP voltage reference for the AGMOPT method.
$V_{\mathrm{AGMPPTref}}$	MPP voltage reference for the AGMPPT method.

I. INTRODUCTION

Maximum peak power tracking (MPPT) with dc–dc converters has been the subject of research in many space programs since its introduction in 1968 [1] because it improves photovoltaic source utilization. It has been of particular interest in LEO satellites due to changes in SA temperature during eclipse and sunlight transitions and in interplanetary probes because of the large variations in irradiance and temperature working conditions. Due to the low photovoltaic power available on small satellites, MPPT techniques become essential functions of their power management and distribution systems [2]. Unlike terrestrial applications, which commonly adopt digital techniques for MPPT, satellites mainly rely on analog circuits to perform PPT and control the dc–dc converters.

Traditionally, MPPT methods for space applications have been designed to operate with uniform power–voltage characteristics with a single MPP. The original method proposed in [1], which has evolved in different implementations [3], [4], [5], [6], describes a boost converter controlled by a flip-flop, which is triggered by the output of two elements that give at their output the difference between the actual current and a fraction of that current and, analogously, the difference between the actual voltage and a fraction of that voltage. It is worth mentioning that this method does not require the computation of the SA power, which was not obvious at that time, and even today is somewhat cumbersome when using space-grade parts.

Another, but simpler, widely used MPPT is the FOCV method [7], which is sustained by the fact that the MPP voltage of a solar cell is proportional to its OC voltage. Due to considerable temperature variations in the space environment, FOCV requires temperature compensation [8]. A slightly different approach is to track the maximum power at the dc–dc converter output. Because the converter output voltage remains constant at the PPT operating frequency, either in a regulated bus electrical architecture or in a battery bus, it can be assumed that the output power tracking becomes the output current tracking. In [9], a maximum output current tracker is used in an unregulated battery bus.

A critical aspect is the implementation complexity, which directly impacts MPPT reliability and power consumption. As an example, space-qualified analog multipliers are scarce and cumbersome to use, so other methods of analog multiplication have been proposed to simplify the overall design. In [10], a PWM multiplier for an analog MPPT is proposed for a cubesat.

A common point to all analog traditional methods and other proposals [11], [12] is that they have been devised for a single MPP and therefore fail to find the GMPP when several local maxima are present in the power–voltage characteristic. In deep space exploration microsatellites, e.g., 6U and 12U cubesats, due to the low irradiance, permanent local maxima can cause a serious risk to the energy balance.

Space is a harsh environment for solar cells. Degradation due to radiation, extreme temperature variations, long satellite lifetime, and micrometeorite impacts can cause solar cells to degrade or malfunction. Solar cell cover glass degradation, irradiance and temperature variations between cells, micrometeorites, and other effects are potential causes of multiple local maxima, and they are common in space environment. Besides, the shadows that the satellite itself can generate on the solar panels, e.g., during maneuvers to change orbit or due to a malfunction of the SA pointing subsystem, can also affect the performance of the SA. It should be noted that the bypass diodes create an additional current path that modifies the power–voltage curve. These and other factors can create complex power–voltage characteristics with multiple local maxima. It is also important to consider that each deep space mission is unique, with completely different conditions for the power system and, therefore, for the SA. Thus, the actual behavior of the solar generator is difficult to predict, not only because of extreme conditions but also because of the lack of heritage in most cases. Depending on the root cause, these local maxima will either disappear once the satellite returns to its correct orientation or they will be permanently reflected in the P–V curve of the SA.

In some terrestrial applications or applications where high reliability is not required, the GMPP problem has already been addressed from a digital perspective. A few examples found in the literature are power–voltage curve scanning in combination with the perturb and observe technique [13], the PSO technique for GMPP tracking [14], and the modified incremental conductance algorithm [15]. However, all these techniques and other digital techniques, such as adaptive perturb and observe [16], are not well suited for high-reliability, robust, and simple global MPPT in space applications. The main reason comes from the fact that they all need a microcontroller or DSP for their implementation, as described in [17]. A basic design principle to guarantee full autonomy of the power system is that the EPS shall not be controlled by programmable devices powered by the EPS itself. On top of that, space-qualified programmable devices, e.g., FPGAs, are usually expensive and power hungry and can experience involuntary reconfiguration due to single-event upsets induced by radiation [18]. Furthermore, a classical method used to calculate the reliability of a system is the parts count method, which is based on the generic failure rates of components, whereby a solution with a minimum number of components has higher reliability [2]. For all these reasons, the preferred solution should consider a simple MPPT algorithm, a discrete implementation, and a reduced number of components with space-grade versions available.

To the authors' knowledge, the only GMPP tracking system devised for space application is the AGMPPT, presented in [19], where a simple way to GMPP tracking using analog circuitry is described for nanospacecraft. It considers input power–voltage curve scanning by charging–discharging the input capacitance of the SAR dc–dc converter. However, neither the detailed implementation nor the experimental results and performance comparison with other methods are presented. On the other hand, using a similar working principle, in this work, a new GMPP tracking method, called AGMOPT is presented. The AGMOPT method is based on scanning the output current sweeping the reference signal of the input voltage loop.

Nowadays, many microsatellite exploration missions, with different scientific objectives, are ongoing or planned by space agencies. Some examples are MarCO, DART, and Solar Cruiser from NASA; M-ARGO, HERA, and LUMIO from ESA; and EQUULEUS from JAXA [20], [21], [22]. In these types of missions, photovoltaic cell degradation is more difficult to predict than in Earth orbit missions, and there is a high level of uncertainty when it comes to establishing the nominal operating conditions. Thus, these are the cases where analog global MPPT methods become relevant. The proposal and comparison of analog global MPPT methods for space applications are rarely discussed in the literature, so their study is necessary and becomes the main contribution of this work. With this in mind, this article aims to show and compare the strengths and weaknesses of the two new GMPP analog methods (AGMPPT and AGMOPT) and compare them with a traditional and well-established method [1], [3], [4], [5], [6]. It is worth noting that there is no previous comparison of peak power trackers for microsatellite missions in the literature. Although in [2], a comparison of MPPT-based EPS architecture for cubesats is presented, it focuses on the electrical architecture and does not include comparisons of the tracking method. Therefore, and due to the great growth in the number of microsatellites launched in recent years, this work is valuable to the scientific community as it is expected to contribute to the design of new SARs for future microsatellites.

The rest of this article is organized as follows. Section II describes the power subsystem and the three MPPT techniques that will be compared. Section III deals with the power system sizing and converter description. Section IV discusses the MPPTs' design guidelines, and Section V describes the experimental setup. Section VI discusses the main results obtained. Finally, Section VII concludes this article.

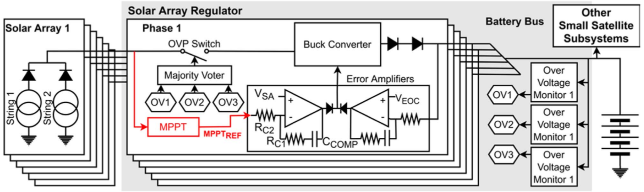

Fig. 1. Block diagram of a small satellite power subsystem (as described in [24]) used as a baseline for MPPT comparatives.

II. SMALL SATELLITE POWER SUBSYSTEM AND PPT

With the advent of miniaturized electrical propulsion systems, small satellites are today capable of performing interplanetary and deep space missions at a lower cost than traditional space missions with larger spacecraft. Within the category of small satellites, cubesats, including all their multiple size variants, have been adopted as a common platform for many academic and research missions and have already been proposed for some lunar and interplanetary missions. Any small satellite requires a hard optimization of the power subsystem in terms of size, mass, and efficiency, eventually ending in simplified electrical bus architecture and complex SA layouts that combine body-mounted and small deployable panels. Regarding the power management architecture [19], unregulated battery bus with MPPT SAR (dc–dc converters) is by far the most common approach, and in many cases, the buck converter is the preferred choice. A typical power conditioning unit [24], which has been considered for this study, is shown in Fig. 1.

The SAR dc–dc converter is a peak-current controlled synchronous buck converter with two outer voltage loops, represented in Fig. 1 as the error amplifier block, that switches from EOC battery voltage regulation to input voltage control for MPP tracking [25]. The reference of the input voltage control loop comes from the MPPT circuit, whereas the reference of the output voltage loop is the battery EOC voltage (V_{EOC}).

A. Analog Oscillating Maximum Power Point Tracking

The working principle of the well-established AMPPT, shown in Fig. 2, is as follows. The MPPT reference signal is a triangular waveform that results from the integration of the R-S flip-flop's output. The SA will oscillate between two points, P_1 and P_2, where the MPP is contained. To explain the principle of operation, let us first consider that the slope of the MPPT reference signal is positive and the SA operating point moves from P_1 to P_2. The SA current decreases until it reaches $k_i{\cdot}I_1$; at this point, a reset in the flip-flop forces a negative slope in the MPPT signal. Furthermore, the flip-flop's output commands the voltage sample and hold circuit, S&H_v, and stores a new $k_v{\cdot}V_2$ limit. Now, in the next part of the cycle, the SA operating point moves from P_2 to P_1 and SA voltage decreases. When the SA voltage reaches $k_v{\cdot}V_2$, the set output of the flip-flop turns ON, the current sample and hold circuit, S&H_i, captures a new limit, $k_i{\cdot}I_1$, the slope of the MPPT reference signal becomes positive, and the cycle repeats.

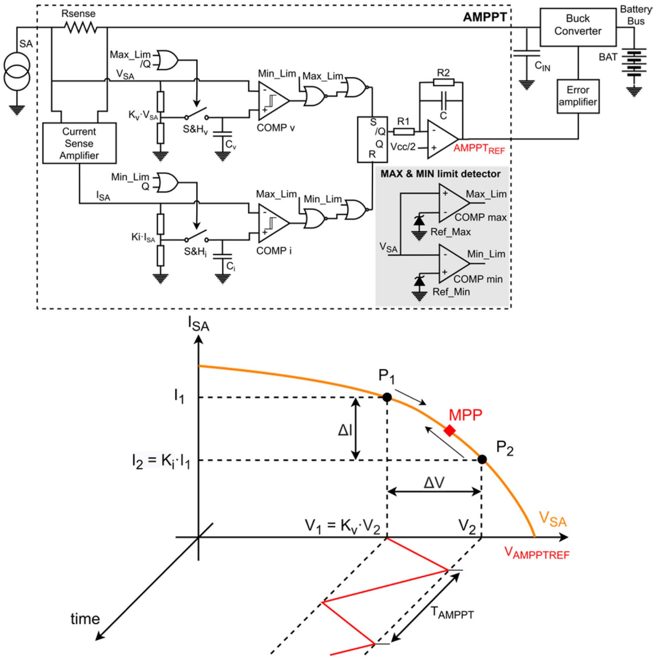

Fig. 2. Block diagram of the proposed AMPPT as the baseline approach for PPT comparatives and a sketch of its operation principle.

Static efficiency is maximized by reducing ΔV and ensuring that $k_v \cdot V_2 < V_{\mathrm{mpp}} < V_2$. The ratio of $\Delta V/\Delta I$ must be chosen considering that at the MPP, $|\Delta V/\Delta I| = V_{\mathrm{mpp}}/I_{\mathrm{mpp}}$ is verified [1], [3]. Increasing the frequency of the triangular MPPT reference signal, f_{AMPPT}, improves the dynamic response; however, it could degrade the static accuracy of the MPPT due to the nonlinear SA parasitic capacitance [26]. The nonidealities of the sample and hold and comparator circuits and sampling capacitors can also deteriorate the static and dynamic performance of the AMPPT. Furthermore, as represented in Fig. 2, maximum and minimum voltage limits must also be defined to force MPPT operation within a specific input voltage range and for start-up purposes. This method oscillates around any local MPP. For a buck converter connected to an SA that exhibits multiple local MPPs on its power–voltage curve, the converter tends to get stuck on the local MPP closest to the V_{OC} after start-up (high-side MOSFET open).

B. Analog Global Maximum Peak Power Tracking

The proposed AGMPPT technique (see Fig. 3) uses the input capacitance of the dc–dc converter, C_{IN}, to scan the SA power–voltage curve and record the SA voltage at the GMPP. The AGMPPT has two different operating states, OFF and MPPT, which are controlled by the clock signal CLK2. During the OFF period (CLK2 = high), the dc–dc converter is disabled, and the batteries must provide power to the bus. During the MPPT interval (CLK2 = low), the dc–dc converter operates at the GMPP.

Focusing on the OFF interval, the first action is to discharge the input capacitor through a current-limited shunt switch. Once C_{IN} is discharged, action commanded by CLK1, it charges again from the photovoltaic source, and the scanning process takes place. SA voltage and current are measured, and SA power is computed using an analog multiplier.

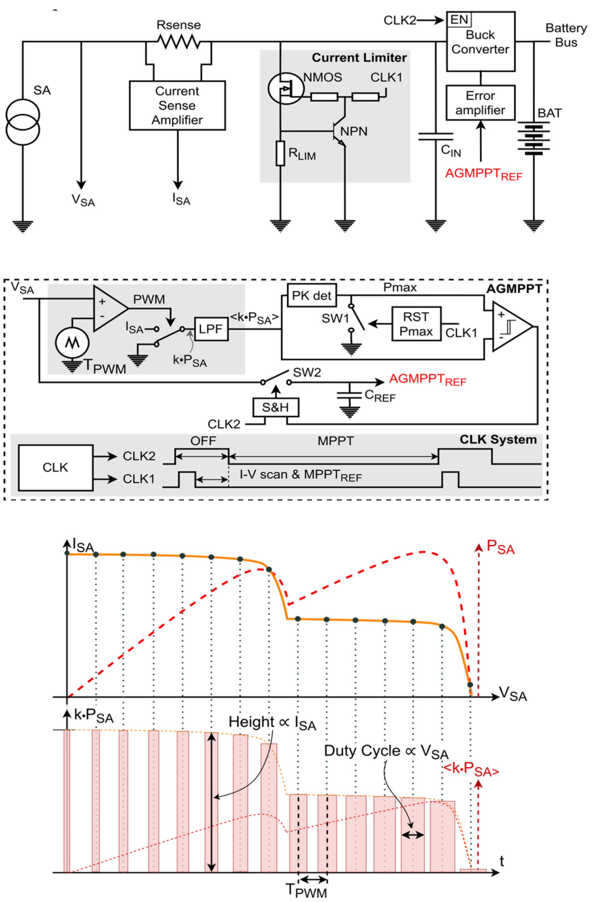

Fig. 3. Block diagram of the proposed AGMPPT for PPT and PWM multiplier operation for SA power computation.

During the scanning phase (CLK1 = low, CLK2 = high), the instantaneous SA power and the maximum SA power obtained from the peak detector circuit are compared. The comparator output signal drives the sample and hold circuit that stores the SA voltage when GMPP occurs, updating the reference of the input voltage loop. Once the OFF-period ends, the dc–dc converter is enabled again, regulating the input voltage at the GMPP. AGMPPT performance is strongly affected by the yield of global peak power acquisition during the scanning period, the ability to maintain the MPPT reference during the MPPT interval, and the AGMPPT duty cycle, $D_{\mathrm{AGMPPT}} = t_{\mathrm{OFF}}/(t_{\mathrm{OFF}} + t_{\mathrm{MPPT}})$. Being the analog multiplier a key element for the proposed AGMPPT, this has been devised as a single-quadrant PWM multiplier followed by an LPF. This approach allows discrete implementation using space-qualified devices. As represented in Fig. 3, V_{SA} is encoded in the duty cycle, whereas I_{SA} is encoded in the signal amplitude of the PWM signal. The LPF removes the carrier frequency and its harmonics.

C. Analog Global Maximum Output Power Tracking

Like the AGMPPT, the novel AGMOPT is also a two-step method, i.e., the SCAN phase and the MOPT phase;

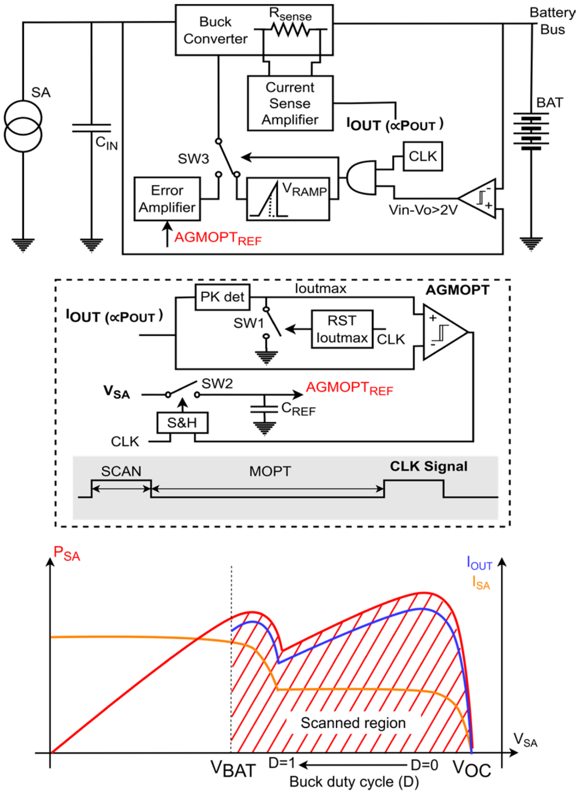

Fig. 4. Block diagram of the proposed AGMOPT for PPT.

however, its operation principle is different. During the SCAN time, the dc–dc converter is operated under peak current control with a varying reference that allows the scan of the SA power–voltage curve. In this method, the scanned region is dc–dc converter topology dependent. For a buck converter operating in CCM, which is considered in this work and commonly found in small satellites, if the duty cycle approaches zero, the SA voltage tends to be an OC voltage. Conversely, when the duty cycle approaches one, the SA voltage clamps to the output voltage, i.e., the battery voltage. However, many PWM controllers limit the minimum (burst mode operation) and maximum duty cycles (due to limitations in high-side MOSFET driving and peak current sensing), further reducing the scanned region.

In an unregulated battery bus topology, if the scan time is short enough, the output voltage remains constant, and the maximum output power can be approximated by the maximum output current. Thus, a simplified but efficient approach is to detect the peak output current during the scan time and store, using a sample and hold circuit, the input voltage reference value at which the maximum output power has been detected, see Fig. 4. Note that the analog multiplier is not needed in this case. During the MOPT phase, the input voltage reference is kept at the value that provides the maximum output current. Due to the structure of the buck converter, the output current is easy to measure with a shunt resistor, and, in fact, many designs include this resistor for current control loop purposes, either in peak current mode or average current mode. Thus, there is no need for additional current-sensing resistors. This is a major difference from AMPPT and AGMPPT methods that require input and output current sense resistors, penalizing the efficiency. Even if the GMPP is outside the scanned region, the maximum available power will be drawn from the dc–dc converter, and this is relevant if the efficiency curves of the dc–dc converter strongly depend on the input voltage, which, in fact, occurs in many cases.

III. POWER SYSTEM SIZING AND CONVERTER DESCRIPTION

To evaluate the different PPT techniques, the irradiance and temperature conditions proposed in [24] have been considered, specifically the irradiance encountered between 1.5 AU (Mars orbit, irradiance Ho = 615 W/m^2) and 2.0 AU (near the asteroid belt, irradiance Ho = 345 W/m^2) and the estimated temperature of the SAs, taking into account the Stefan–Boltzmann law and spacecraft heat. Due to the long travel distance, the maximum power of the photovoltaic source is always necessary to achieve the required propulsion, and thereby the MPPT technique should be optimized for slow but wide variations in the power–voltage curve of the SA. A total of 120 triple junction cells (Azurspace 3G30C, [27]) are organized in 12 strings of 10 cells in series. Each SAR module accommodates two solar cell strings, processing between 6.81 W (2.0 AU) and 9.65 W (1.5 AU).

The following six different power–voltage curves covering different mission scenarios have been selected.

1) Uniform — single MPP at 1.5 AU,
2) Uniform — single MPP at 2.0 AU,
3) Nonuniform 1 at 1.5 AU — two local MPP and GMPP closest to the SA SC point,
4) Nonuniform 1 at 2.0 AU — two local MPP and GMPP closest to the SA SC point,
5) Nonuniform 2 at 1.5 AU — two local MPP and GMPP closest to the SA OC point,
6) Nonuniform 2 at 2.0 AU — two local MPP and GMPP closest to the SA OC point.

As indicated above, these power–voltage curves are obtained by considering an SA with two strings in parallel, each with ten cells in series (10S2P). In scenarios 1 and 2, no degradation is considered. In scenarios 3 and 4, a degradation of three cells in one string has been considered. Finally, in scenarios 5 and 6, degradation of five cells in one string has been considered. A representation of those curves is shown in Fig. 5. The battery is made up of 12 Li-ion cells (SAFT 174865xlr, [27]) organized in 3 strings of 4 cells in series. The battery bus voltage varies from 12.8 to 16.8 V.

In accordance with common space design practice and the specific mission type, the following design constraints have been considered.

1) Illumination and temperature vary in a wide range, and these changes have been considered at the solar cell level. Furthermore, cell shadowing is a potential problem due to the complex structure of body-mounted and deployable panels and the mission profile.

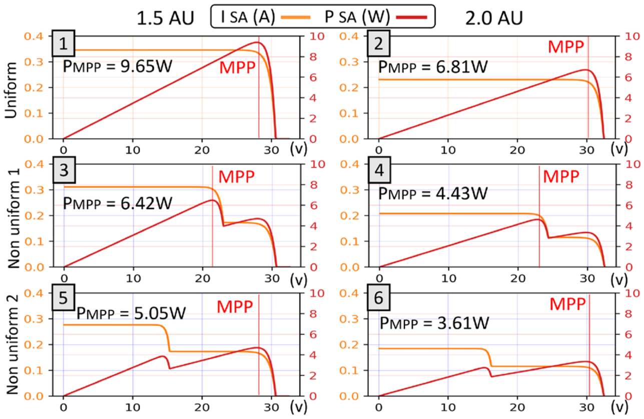

Fig. 5. Power–voltage curves used for comparison of different PPT techniques.

2) Part list must be minimized, and only radiation hardened components must be considered for the final design.
3) DC–dc conversion and PPT must perform satisfactorily under all circumstances, but they are critical under low-power and low-current conditions (2.0 AU).
4) Each design should be optimized for the best performance in terms of maximum bus power and minimum power consumption, which could require some additional considerations, such as changes in the power converter values and different MPPT frequencies for each method.

As the main SAR converter, a dc–dc buck converter has been designed following the ESA standards [29], [30]. This converter uses the LT3845 PWM controller from Analog Devices. The main reason for using this controller is because there is a space-qualified version, the RH3845MK. The LT3845 implements an internal peak current control loop and an antislope compensation circuit that removes the current limit associated with slope compensation at high duty cycles. The output of the internal transconductance error amplifier is configured so that it can be manipulated by an external control loop. In this case, the outer control loop is a voltage loop that uses the voltage reference provided by the MPPT circuits as a reference. The converter, which is sized for supplying 10 W, has a switching frequency of 125 kHz, and in order to minimize current ripple at the output, it uses a 470-μH inductor and a 44-μF capacitor.

Knowing the dc–dc converter efficiency under steady-state conditions, without any PPT method, at points that correspond to the GMPP for each scenario, is of paramount importance to evaluate the three different MPPT methods. These results have been summarized in Table I, and it can be observed that the efficiency varies from 66% to 88%, degrading the performance at lower input power.

IV. DESIGN GUIDELINES OF THE PROPOSED PPT METHODS

This section describes the most relevant design aspects of each PPT method.

TABLE I
SAR Converter Efficiency (%) $V_{\mathrm{BATT}} = 16.8$ V

		P_{IN} (W)	P_{OUTmax} (W)	Eff. (%)
	$V_{\mathrm{BATT}} = 16.8$ V			
1.5 AU	Uniform	9.65	8.39	86.94
	Nonuniform 1	6.42	5.51	85.82
	Nonuniform 2	5.05	3.88	76.83
2.0 AU	Uniform	6.81	5.77	84.73
	Nonuniform 1	4.43	3.66	82.61
	Nonuniform 2	3.61	2.54	70.36
	$V_{\mathrm{BATT}} = 12.8$ V			
		P_{IN} (W)	P_{OUTmax} (W)	Eff. (%)
1.5 AU	Uniform	9.65	8.42	87.25
	Nonuniform 1	6.42	5.61	87.38
	Nonuniform 2	5.05	4.07	80.59
2.0 AU	Uniform	6.81	5.66	83.11
	Nonuniform 1	4.43	3.53	79.68
	Nonuniform 2	3.61	2.38	65.92

TABLE II
AMPPT Efficiency (%)

Kv, Ki	1.5 AU Uni	2.0 AU Uni	1.5 AU nU2	2.0AU nU2	AVG
0.905	0.951	0.925	0.916	0.959	0.938
0.913	0.954	0.928	0.923	0.962	0.941
0.921	0.957	0.931	0.924	0.965	0.944
0.933	0.961	0.934	0.929	0.967	0.948
0.944	0.966	0.937	0.934	0.969	0.951
0.953	0.968	0.941	0.936	0.974	0.955
0.964	0.973	0.945	0.940	0.967	0.958
0.977	**0.977**	**0.950**	**0.943**	**0.982**	**0.963**
0.989	0.979	0.904	0.948	0.919	0.938
0.995	0.910	0.772	0.948	0.919	0.831

The bold entities indicate the corresponds to the maximum average value.

A. AMPPT Circuit Design

Although the AMPPT method is simple in its conception, its design is not. The main reason is that the selection of K_v and K_i is highly dependent on the SA current–voltage curve, and this curve considerably varies throughout the mission's lifetime. At the furthest point, 2.0 AU, the SA current is the lowest (the solar constant is inversely proportional to the square of the Sun's distance), and the OC voltage is the maximum (the temperature is minimum). Ideally, the closer K_v and K_i are to one, the better the static efficiency; however, there are hardware limitations that eventually ask for fine-tuning using the experimental prototype.

The design procedure followed in this work could be summarized as follows.

Step 1: K_v and K_i definitions. SA power–voltage curve numbers one, two, five, and six are considered (curves three and four are discarded since GMPP is not tracked). K_v and K_i must be equal to have almost the same power at P_1 and P_2, as shown in Fig. 2. The optimum value has been obtained experimentally, refer to Table II, and results $K_v = K_i = 0.977$.

Step 2: MPPT frequency selection. It can be adjusted up to several tens of hertz according to the crossover frequency of the input voltage loop; however, to avoid any problem with the dynamic response of the SA [23], the MPPT frequency has been limited to $f_{\mathrm{AMPPT}} = 16$ Hz, which corresponds to the following component values: $R1 = 240$ kΩ, $R2 = 80$ kΩ and $C = 4.7$ μF (refer to Fig. 2).

TABLE III
DC–DC Converter Main Parameters for Each PPT Configuration

	AMPPT	***AGMPPT***	***AGMOPT***
Input Capacitance (C_{IN})	30 μF	128 μF	7.5 μF
Comp. Capacitor (C_{COMP})	10 nF	18 nF	4.7 nF
Comp. Gain (R_{C1}/R_{C2})	3.84	7.50	1.83
Out. Current Sense Resistor (R_O)	50 mΩ	50 mΩ	80 mΩ
In. Current Sense Resistor (R_I)	200 mΩ	200 mΩ	N/A
Output Inductance (L_O)	470 μH		
Switching Frequency (fs)	125 kHz		
Input Voltage Loop Crossover Frequency (fc_{VIN})	MIN: 859 Hz (128 μF 2 AU, 12.8V_{EOC}) MAX: 2860 Hz (7.5 μF, 2 AU, 16.8V_{EOC})		
MPPT Period	60 ms	2 s	12 s
Scanning time	N/A	42 ms	< 250 ms

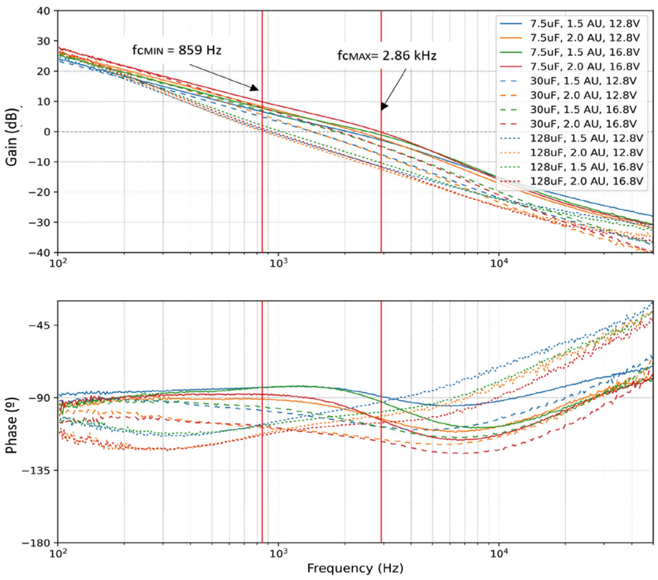

Fig. 6. Measured input voltage loop gain, $T_{\mathrm{Vin}}(s)$, for different C_{IN} capacitors, *P–V* curves, and battery voltages.

Step 3: Max and Min limits. The maximum and minimum limits have been established as 95% of the greatest SA voltage and 105% of the battery voltage, respectively.

Step 4: Converter input capacitance $C_{\mathrm{IN}} = 30\ \mu$F, input current sense resistor $R_{\mathrm{SENSE}} = 200$ mΩ, and compensator values are chosen to achieve a crossover frequency of the input voltage loop between 2 and 3 kHz and a phase margin greater than 60° over the full range of possible conditions during the mission, as detailed in [31]. Compensator values are included in Table III. The input voltage control loop gain has been measured, and it is shown in Fig. 6.

B. AGMPPT Circuit Design

The main design consideration is the AGMPPT duty cycle, defined as $D_{\mathrm{AGMPPT}} = t_{\mathrm{MPPT}}/(t_{\mathrm{OFF}}+t_{\mathrm{MPPT}})$, because it directly defines the maximum theoretical efficiency. Increasing t_{MPPT} will increase D_{AGMPPT} by reducing the MPPT refreshing frequency, $f_{\mathrm{AGMPPT}} = 1/(t_{\mathrm{OFF}}+t_{\mathrm{MPPT}})$. Obviously, this is not an optimal solution if power–voltage characteristics change rapidly, and it also poses some additional complications to the sample and hold circuit that maintains the AGMPPT voltage reference. However, increasing t_{MPPT} has the beneficial effect of reducing the number of dc–dc converter interruptions and, indirectly, reduces the hysteresis problem of SAs [23], since t_{OFF} can be augmented proportionally. When focusing on t_{OFF}, the scanning process and analog power multiplication are the two critical design issues. The input capacitance of the dc–dc converter is mainly determined by the input voltage ripple and the input voltage loop stability requirements. For a given SA power–voltage curve, small values of the input capacitance will reduce the required scan time, and less energy will be dissipated in the current-limiting switch when it is discharged; however, it demands larger bandwidth in the analog multiplier and peak detector circuits. Low part count and low power consumption are also very important design constraints for such low-power processing dc–dc converters, especially at 2.0 AU. The accuracy and stability of the AGMPPT reference signal are also critical. Near any local MPP, the peak power value and instantaneous power get very close, which compels a very precise comparator to minimize the amount of hysteresis required to prevent oscillations in the sample and hold switch. Furthermore, the holding circuit requires very low leakage currents (I_{LEAK}) to maintain a stable AGMPPT reference voltage during t_{MPPT}.

The AGMPPT design procedure is an iterative method that can be summarized as follows.

Step 1: t_{OFF} selection. AGMPPT duty cycle defines the maximum theoretical efficiency, so the lowest t_{OFF} becomes the best. However, the dc–dc converter input capacitance and maximum allowed dP_{SA}/dt during the scanning period should be considered. The PWM multiplier carrier frequency has been set to 500 kHz, and the first-order LPF cutoff frequency is 7.5 kHz (i.e., time delay = 21 μs). Considering all the SA power–voltage curves shown in Fig. 5, it has been experimentally observed that a $C_{\mathrm{IN}} = 128\ \mu$F gives a maximum $|dP_{\mathrm{SA}}/dt|$ around 5000 W/s that implies a reduction of less than 1% of maximum power due to analog multiplication delay. Once C_{IN} is determined, $t_{\mathrm{OFF}} > C_{\mathrm{IN}} \cdot V_{\mathrm{OCmax}}/I_{\mathrm{SCmin}}$ must be fulfilled. Thus, in this case, $t_{\mathrm{OFF}} = 43$ ms is chosen.

Step 2: AGMPPT period definition. The upper limit is restricted by the V_{MPP} variation over time, which depends on mission considerations. The lower limit is defined by the maximum frequency of the AGMPPT, which is linked to the SA characteristics, the dc–dc input capacitor, the number of allowable dc–dc interruptions, and the hysteresis associated with the SA during the scanning process. In this case, an optimum value has been experimentally identified as $T_{\mathrm{AGMPPT}} = 2$ s, and eventually, $D_{\mathrm{AGMPPT}} \cong 98\%$ is obtained.

Step 3: AGMPPT reference capacitor selection ($C_{\mathrm{REFAGMPPT}}$). A stable AGMPPT voltage reference is required during t_{MPPT}. The main contributors for the AGMPPT reference capacitor discharge are the sample and hold switch leakage current, the input leakage current of the buffer stage, and the own capacitor leakage current. Thus, $C_{\mathrm{REFAGMPPT}} > \Sigma I_{\mathrm{LEAK}} \cdot t_{\mathrm{MPPT}}/\Delta V_{\mathrm{AGMPPTref}}$ must be satisfied. Considering $\Delta V_{\mathrm{AGMPPTref}} < 5\mathrm{mV}$, $t_{\mathrm{MPPT}} = 1.96$ s, and $\Sigma I_{\mathrm{LEAK}} < 20$ nA, $C_{\mathrm{REF\ AGMPPT}} = 20.4\ \mu\mathrm{F}$ ($3 \times 6.8\mu\mathrm{F}$) is obtained.

Step 4: Input voltage control loop adjustment. Since the input capacitance has been increased for scanning purposes (step 1), the error amplifier values have been changed to keep the similar performance as the AMPPT prototype. Compensator values and input voltage loop gain are included in Table III and Fig. 6, respectively.

To summarize, it is worth noting that the shorter the scan time, the more complex the design of the critical functions, i.e., the PWM multiplier, peak power detector, and sample and hold circuit. A balance in circuit complexity and part count is necessary to keep a small PCB area and, more importantly, low power consumption of the AGMPPT circuit.

C. AGMOPT Design

The AGMOPT adjusts the dc–dc control signal to determine the optimum operation point. Therefore, the AGMOPT performance is tightly linked to the dc–dc converter characteristics. As with the AGMPPT, the AGMOPT duty cycle is the main design driver, $D_{\mathrm{AGMOPT}} = t_{\mathrm{MOPT}}/(t_{\mathrm{SCAN}} + t_{\mathrm{MOPT}})$. In a buck converter, as considered in this study, during the SCAN period, the power processed by the converter varies from zero to a certain power defined by the battery voltage and the SA power–voltage curve, whereas in the MOPT phase, the maximum output current is supplied to the bus. Thus, the higher D_{AGMOPT} the better the theoretical efficiency. Another relevant aspect is the output current filtering. In a buck converter operating in CCM, the output current requires little filtering effort, reducing measurement delay and simplifying filter design. Furthermore, filtered output current exhibits a fairly flat response around the maximum output power point, making peak power detection difficult. Finally, the maximum duty cycle must be limited to avoid protection triggering of the dc–dc converter and peak current loop instability.

The AGMOPT design procedure can be summarized as follows.

Step 1: Adjust C_{IN}. Input voltage loop bandwidth, as can be observed in Fig. 6, strongly depends on C_{IN}. Reducing C_{IN} will provide a faster response and, consequently, t_{SCAN} could be reduced. This means that D_{AGMPOT} increases for a particular T_{AGMOPT}. In this case, $C_{\mathrm{IN}} = 7.5\mu\mathrm{F}$ assures an $\mathrm{fc}_{\mathrm{vin}} > 2$ kHz, which means an approximate rise time, $\mathrm{tr}_{\mathrm{vin}} < 175\ \mu\mathrm{s}$.

Step 2: Determination of the control signal ramp. The slew rate of the control signal, which defines the t_{SCAN}, should be selected depending on the crossover frequency of the dc–dc converter input voltage loop, $\mathrm{fc}_{\mathrm{vin}}$. The maximum value of the ramp must be dynamically changed with converter input and output voltages. The control signal ramp is designed to fulfill $\mathrm{tr}_{\mathrm{vin}}/t_{\mathrm{ramp}} < 1\%$ to limit the delay during the scanning, defining a control signal ramp time, $t_{\mathrm{ramp}} < 250$ ms. The control ramp ends when $V_{\mathrm{IN}} = V_O + 2V$.

TABLE IV
PPT Part List

Part	***Number of parts***		
	AMPPT	*AGMPPT*	*AGMOPT*
Resistors	26	32	28
Capacitors	25	25	14
Logic gates	8	9	3
BJT Transistor	0	2	1
Comparators	4	2	3
Diodes/Zeners	3	2	6
Analog switches	2	3	3
Flip-flops	1	0	0
Timer ICs	0	2	1
Op. Amplifier	4	4	2
Current sensor	2	2	1
Shunt resistor	1	1	0
MOSFETs	0	2	1
Total number of parts:	**76**	**86**	**63**

Step 3: Determination of T_{AGMOPT}. This has been selected to achieve $D_{\mathrm{AGMOPT}} \cong 98\%$ as in the case of the AGMPPT, obtaining $T_{\mathrm{AGMOPT}} = 12$ s. To maintain $\Delta V_{\mathrm{AGMOPTref}} < 30\mathrm{mV}$, assuming ΣI_{LEAK} similar to that obtained in the AGMPPT, the reference capacitor $C_{\mathrm{REF\ AGMOPT}} = 33\ \mu\mathrm{F}$.

Step 4: Output current filter. A low-pass first-order filter is used to remove switching and harmonic content from the converter output inductor current. The filter cutoff frequency is selected to be half the switching frequency, $\mathrm{fc}_{\mathrm{io}} = f_{\mathrm{sw}}/2 = 62.5$ kHz.

Step 5: Input voltage control loop adjustment. Since the input capacitance has been decreased (step 1), the error amplifier values have been changed to keep the similar performance as the AMPPT prototype. Compensator values and input voltage loop gain are included in Table III and Fig. 6, respectively. Note that in this case, an input current sense resistor is not needed, since the buck converter output current sense resistor is used, which has been slightly increased to improve measurement accuracy.

Table III shows the main parameters of the buck converter used in each PPT configuration, as well as the main parameters of the PPT used. The measured input voltage loop gain for each converter configuration is shown in Fig. 6, showing that converter stability and dynamic response remain similar in all three cases.

The part count of the three peak power trackers, classified by groups, has been presented in Table IV. It is observed that AGMOPT requires less parts, favoring area reduction and cost reduction.

V. PROTOTYPE DESIGN AND TEST SETUP IMPLEMENTATION

To evaluate the proposed methods and carry out the pertinent tests, a six-phase SAR prototype, as shown in Fig. 1, is used. The original AMPPT is implemented on the SAR board, whereas the AGMPPT and AGMOPT are externally connected, refer to Fig. 7. It should be noted that in the AGMPPT and AGMOPT prototypes, different connectors and test pins have been included. To have a more

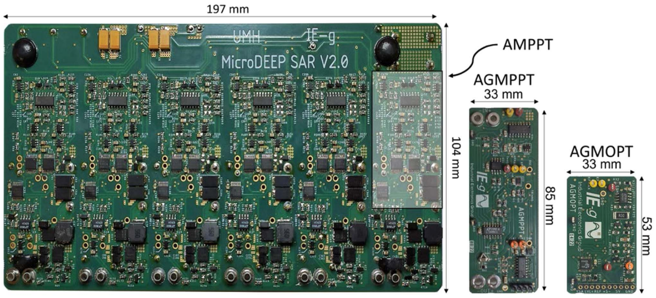

Fig. 7. Experimental prototypes. Left: six-phase SAR with AMPPT. Center: AGMPPT board. Right: AGMOPT board.

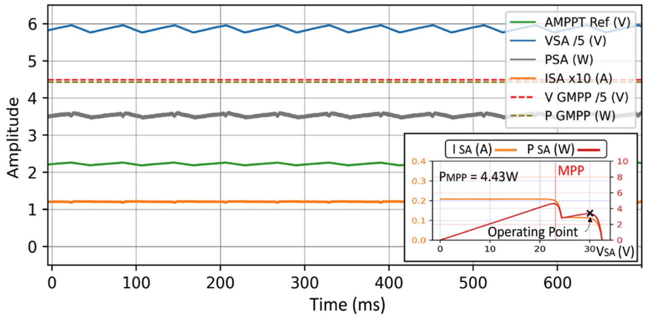

Fig. 8. AMPPT at 2.0 AU, nonuniform 1 SA *P*–*V* curve, $V_{\mathrm{BATT}} =$ 12.8 V.

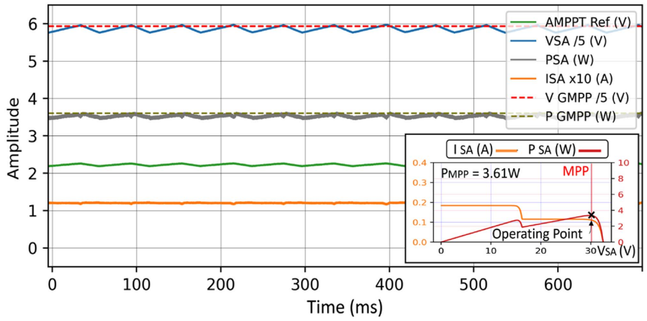

Fig. 9. AMPPT at 2.0 AU, nonuniform 2 *P*–*V* curve, $V_{\mathrm{BATT}} = 12.8$ V.

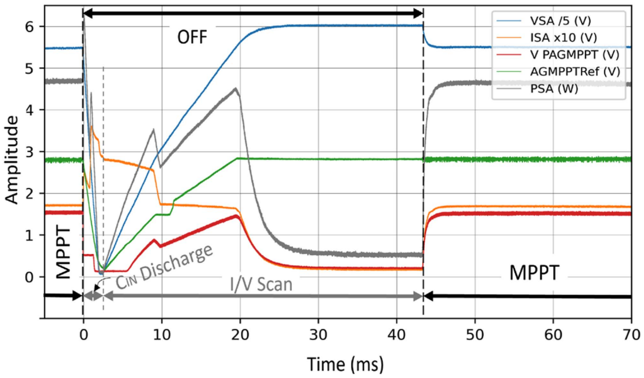

Fig. 10. AGMPPT at 1.5 AU, nonuniform 2 *P*–*V* curve, $V_{\mathrm{BATT}} =$ 12.8 V.

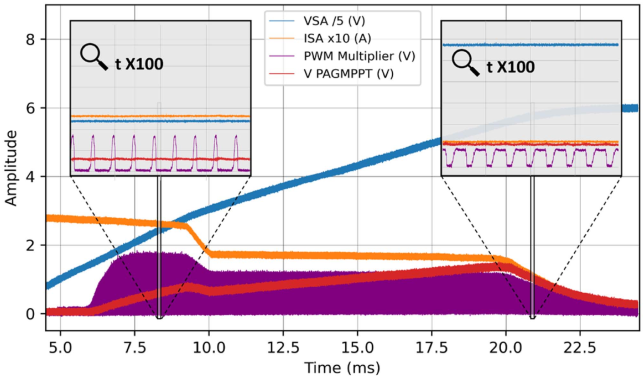

Fig. 11. PWM multiplier operation: a detailed view of the SCAN phase (AGMPPT at 1.5 AU, nonuniform 2 *P*–*V* curve, $V_{\mathrm{BATT}} = 12.8$ V).

confident reference in terms of the surface area required for each PPT method, the number of components required to implement each of the three systems has been taken as a criterion, as presented in Table IV.

The six SA power–voltage curves have been simulated with two computer-controlled Agilent E4351B SA simulators connected in parallel. An ITECH IT-M3412 battery simulator is used. Tektronix DPO 4034 oscilloscope, Tektronix TPP1000 voltage probes, and Tektronix TCP0030A current probes are used for waveform acquisition with post-processing Python scripts for results representation. A Rigol DP831 power supply and a Fluke 8846A multimeter have been used to perform current consumption tests.

VI. EXPERIMENTAL RESULTS

The first batch of tests shows the operation principle of each method. Figs. 8 and 9 show the most representative signals of the AMPPT during its operation. It is observed that signals are continuously oscillating, and no scanning process takes place with this method. Furthermore, it is clearly recognized that AMPPT gets trapped in a local MPP in Fig. 8, i.e., it oscillates around the local MPP closest to V_{OC}, and it works properly in Fig. 9. This also happens with nonuniform curve 1 at 1.5 AU.

Fig. 10 shows the AGMPPT operation. Before $t = 0$ s, the SAR operates in the MPPT mode. At $t = 0$ s, C_{IN} discharges for 3 ms; then, the *I*–*V* scan phase starts and takes around 40 ms. During this phase, it is observed that V_{SA} moves from 0 to V_{OC}, the *P*–*V* curve is computed analogously, and the $V_{\mathrm{AGMPPTref}}$ is properly sampled and retained in the GMPP. At $t = 43$ ms, a new MPPT phase starts.

A zoomed view of the scanning process and the PWM multiplier operation is shown in Fig. 11. In the first zoomed area, at around $t = 8$ ms, the PWM signal (purple trace) has a low duty cycle (low SA voltage) and large amplitude (large SA current). However, in the second zoomed area, at around $t = 21$ ms, the PWM signal exhibits a high duty cycle but low amplitude. The filtered PWM signal (red trace) ultimately mimics the SA *P*–*V* curve, where the two local MPPs are clearly identified.

In Figs. 12 and 13, several cycles of the AGMPPT technique are shown for nonuniform curves 1 and 2, respectively, at 2.0 AU and $V_{\mathrm{BATTERY}} = 12.8$ V. It is clearly observed that GMPP tracking is properly achieved

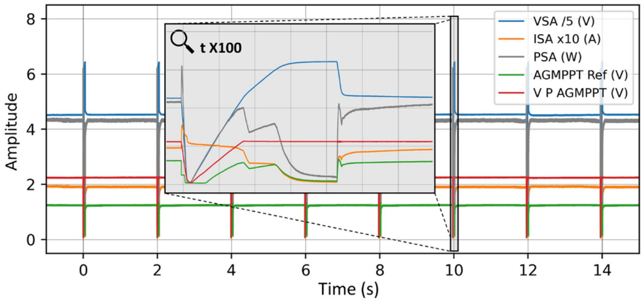

Fig. 12. AGMPPT at 2.0 AU, nonuniform 1 *P*–*V* SA curve, $V_{\mathrm{BATT}} =$ 12.8 V.

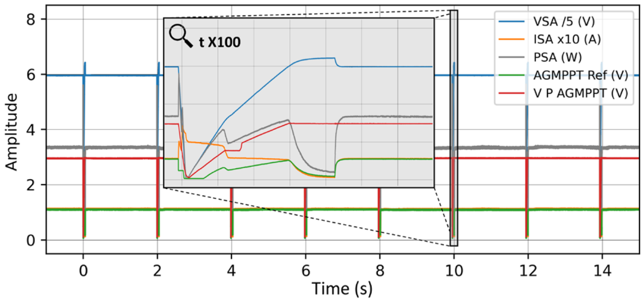

Fig. 13. AGMPPT at 2.0 AU, nonuniform 2 *P*–*V* SA curve, $V_{\mathrm{BATT}} =$ 12.8 V.

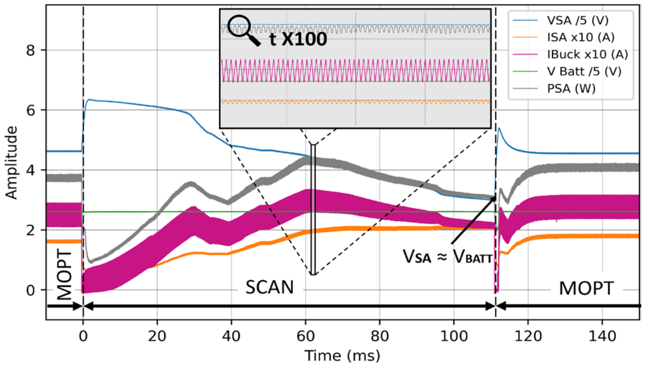

Fig. 14. AGMOPT at 2.0 AU, nonuniform 1 *P*–*V* SA curve, $V_{\mathrm{BATT}} =$ 12.8 V.

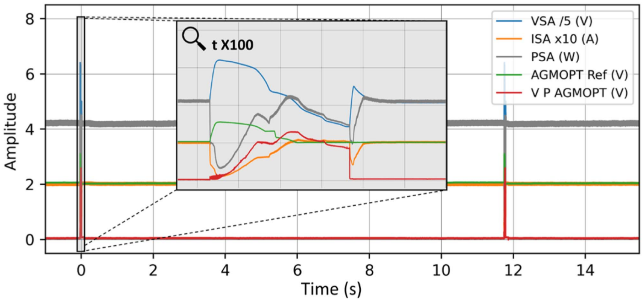

Fig. 15. AGMOPT at 2.0 AU, nonuniform 1 *P*–*V* SA curve, $V_{\mathrm{BATT}} =$ 12.8 V.

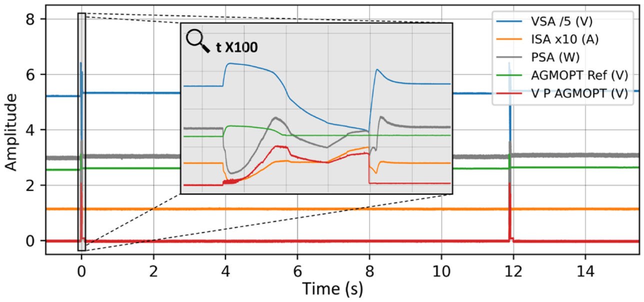

Fig. 16. AGMOPT at 2.0 AU, nonuniform 2 *P*–*V* SA curve, $V_{\mathrm{BATT}} =$ 12.8 V.

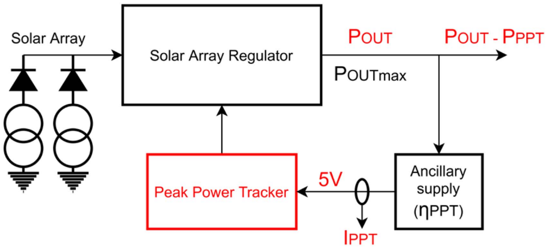

Fig. 17. PPT efficiency setup measurement.

in both curves and V_{SA} at GMPP does not drift during $T_{\mathrm{AGMPPT}} = 2$ s. Thus, maximum SA power is extracted regardless of the environmental conditions and complex *P*–*V* curves.

The AGMOPT operation principle is shown in Fig. 14. Before $t = 0$ ms, the SAR is in the MOPT mode. At $t = 0$ s, the scan process starts. Since the control reference signal V_{RAMP} starts at zero volts, the SA operating point starts from SA V_{OC}. Next, as the V_{RAMP} rises, the output current increases, and the SA operating point moves toward the SA SC operating point. The scan interval ends when V_{SA} is close to battery voltage, $t = 110$ ms, which is clearly noted since output current ripple ΔI_{BUCK} reduces. It is also worth to mention that I_{BUCK} remains proportional to SA power and the battery voltage is constant during the scan period. Filtering I_{BUCK} and capturing the voltage at the maximum current will provide the voltage $V_{\mathrm{AGMOPTref}}$ for the next MOPT interval.

To conclude with the first batch of measurements, two cycles of the AGMOPT method are represented in Figs. 15 and 16 for nonuniform curves 1 and 2, respectively, at 2.0 AU and $V_{\mathrm{BATTERY}} = 12.8$V. It is clearly shown that GMPP is correctly tracked in both curves.

The second batch of tests has been devised to determine the efficiency (η) of each PPT method for each *P*–*V* curve and the minimum (12.8 V) and maximum (16.8 V) battery voltages. As illustrated in Fig. 17, the efficiency has been defined as the ratio between the actual output power P_{OUT} minus the ancillary power required for the PPT circuit P_{PPT} and the maximum output power P_{OUTmax}, which is obtained by varying the converter control signal (without any PPT circuit) until maximum output power is detected for each configuration of *P*–*V* curve and battery voltage. P_{PPT} is defined as $P_{\mathrm{PPT}} = 5\ \mathrm{V}{\cdot}I_{\mathrm{PPT}}/\eta_{\mathrm{PPT}}$, where 5 V is the ancillary MPPT voltage supply, I_{PPT} is the current consumption of the whole MPPT circuit, and η_{PPT} is the ancillary MPPT voltage regulator efficiency. Measured

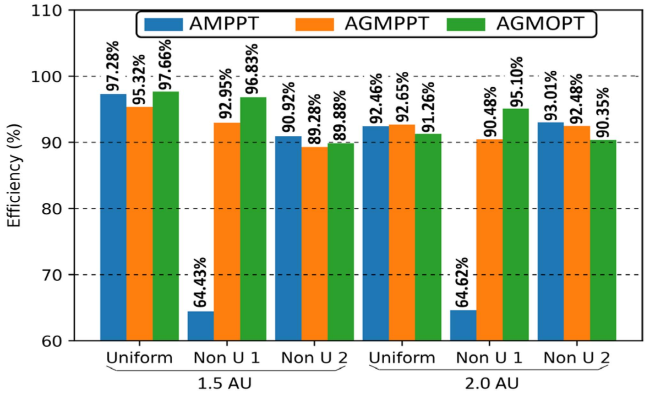

Fig. 18. AMPPT, AGMPPT, and AGMOPT efficiency results, $V_{\mathrm{BATT}} = 12.8$ V.

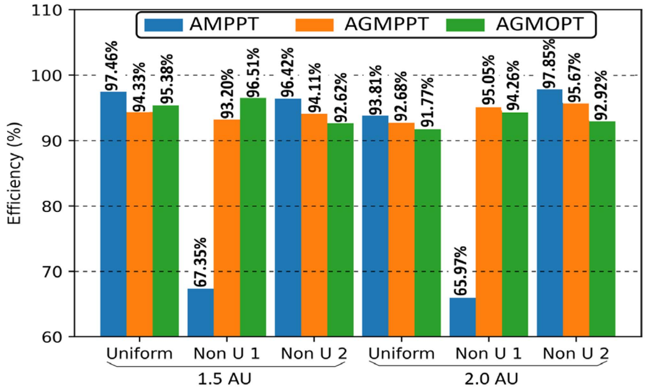

Fig. 19. AMPPT, AGMPPT, and AGMOPT efficiency results, $V_{\mathrm{BATT}} = 16.8$ V.

I_{PPT} are 21.9 mA for AMPPT, 29.2 mA for AGMPPT, and 18.8 mA for AGMOPT, and $\eta_{\mathrm{PPT}} = 80\%$ is considered.

Figs. 18 and 19 represent the efficiency results obtained for $V_{\mathrm{BATTERY}} = 12.8$ V and $V_{\mathrm{BATTERY}} = 16.8$ V, respectively. It can be concluded that the AMPPT is the most efficient method when the GMPP is located closer to the V_{OC}, which corresponds to the uniform and nonuniform 2 curves, achieving a peak efficiency of 97.8% at 2.0 AU and $V_{\mathrm{BATT}} = 16.8V$.

However, the AMPPT suffers a large efficiency drop in nonuniform 1 curves, remaining below 68% in all cases, which limits its use if multiple local MPPs are expected during the mission. AGMPPT and AGMOPT maintain high efficiency in all cases and when compared to each other, but there is no clear winner in terms of averaged efficiency, $\Sigma\eta_{\mathrm{AGMPPT}}/12 = 93.2\%$ and $\Sigma\eta_{\mathrm{AGMOPT}}/12 = 93.7\%$, and other considerations should be pondered for a final selection (e.g., total number of parts, PPT refreshing rate, dc–dc converter requirements, or any other).

VII. CONCLUSION

In this work, three different analog peak power trackers have been designed and evaluated for small satellite missions, more specifically for ones where complex SA power–voltage curves are expected. Two novel analog power optimizer methods, AGMPPT and AGMOPT, are compared with the well-established analog oscillating MPPT. It is demonstrated that in uniform conditions, the traditional method exhibits the best performance in terms of efficiency and assures smooth operation of the SAR and battery. However, the AMPPT fails when several local maxima are present in the power–voltage curve, and it only works properly if the GMPP is closer to the OC voltage of the SA. The AGMPPT exhibits higher circuit complexity but better performance in GMPP tracking where the AMPPT fails, but efficiency is penalized in uniform power–voltage characteristics and when AMPPT correctly finds the GMPP. Furthermore, it produces periodic connection and disconnection of the SAR, causing transient battery charge and discharge. An additional interesting feature that could be exploited is that the SA power–voltage curve is available for telemetry purposes. The last method AGMOPT is the simplest arrangement, and it also considers the efficiency of the dc–dc converter. Since it perturbs the operation point to locate the maximum output power, the battery is exposed to constant charge and discharge. The main drawback of this approach is the difficulty of precise output current tracking, which results in a reduction in efficiency. However, this is in part compensated by less consumption of the PPT circuits. It also requires a longer refreshing frequency, since it strongly depends on the bandwidth of the input voltage control loop.

Regarding the tracking time, defined as the maximum time required by the PPT method to obtain the GMPP after a change in the SA curve occurs, the AGMPPT has a fixed tracking time of 2 s, and the tracking time of the AGMOPT is 12 s. The tracking time of the AMPPT method depends on the initial MPP point as well as the new MPP point, which is 1.2 s in the worst case (estimated by computer simulation). However, it should be noted that the transition between MPPs goes smoothly. In this regard, transient local maxima whose duration is less than the MPPT tracking time will not be detected. However, local maxima with longer durations will affect the satellite's power balance, and the proposed methods will extract the maximum available energy. It is worth to mention that tracking time is not so critical when compared with the variation of the irradiance and temperature in a deep space mission, whose time scale is much longer.

As to the computation time, which corresponds to the scanning time, i.e., the time required by each of the methods to determine where the MPP is located, the AMPPT does not perform the scanning process, while the computation time is 42 ms and 250 ms for the AGMPPT and AGMOPT, respectively.

As the electronic parts used are very common discrete analog parts, it can be concluded that the differences in terms of volume, weight, or unit cost between the three proposed methods are negligible with respect to the total mass of the entire satellite, not being a real limitation for the final selection of any of the three methods. Thus, a final selection depends on multiple considerations, such as power system architecture or dc–dc converter topology.

TABLE V
Summary of Main Features

Feature	***MPPT Method***		
	AMPPT	AGMPPT	AGMOPT
Number of parts	76	86	63
Relative unit cost, size, and mass*	1	1.13	0.83
MPPT circuit power consumption	0.110 W	0.146 W	0.094 W
Average efficiency (with local MPP)	85.13 %	93.2 %	93.7 %
Average efficiency (without local MPP)	95.25 %	93.74 %	94.02 %
Tracking time (worst case)	1.2 s	2 s	12 s
Scanning time	N/A	42 ms	>250 ms

* Relative to the AMPPT, based on the number of components required for each implementation.

Finally, Table V summarizes the main characteristics of the proposed MPPTs. These methods can be upgraded to space-qualified designs.

REFERENCES

[1] A. F. Boehringer, “Self-adapting dc converter for solar spacecraft power supply selbstanpassender gleichstromwandler für die energieversorgung eines sonnensatelliten,” *IEEE Trans. Aerosp. Electron. Syst.*, vol. AES-4, no. 1, pp. 102–111, Jan. 1968, doi: 10.1109/TAES.1968.5408938.

[2] A. Edpuganti, V. Khadkikar, H. Zeineldin, M. S. E. Moursi, and M. Al Hosani, “Comparison of peak power tracking based electric power system architectures for CubeSats,” *IEEE Trans. Ind. Appl.*, vol. 57, no. 3, pp. 2758–2768, May/Jun. 2021, doi: 10.1109/TIA.2021.3055449.

[3] W. Denzinger, “Electrical power system of Globalstar,” in *Proc. 4th Eur. Space Power Conf.*, 1995, pp. 171–174.

[4] H. Jansen and J. Laursen, “Power conditioning unit for Rosetta/Mars express,” in *Proc. 6th Eur. Space Power Conf.*, 2002, p. 249, ESA SP-502.

[5] J.-E. Park, J.-K. Han, K.-B. Park, B.-H. Lee, and G.-W. Moon, “A new direct charging control for electrical power systems in low Earth orbit satellites,” *IEEE Trans. Aerosp. Electron. Syst.*, to be published, doi: 10.1109/TAES.2022.3218495.

[6] D. Selcan, G. Kirbis, and I. Kramberger, “Analog maximum power point tracking for spacecraft within a low earth orbit,” *IEEE Trans. Aerosp. Electron. Syst.*, vol. 52, no. 1, pp. 368–378, Feb. 2016, doi: 10.1109/TAES.2015.140279.

[7] J. J. Schoeman and J. D. van Wyk, “A simplified maximal power controller for terrestrial photovoltaic panel arrays,” in *Proc. IEEE Power Electron. Specialists Conf.*, 1982, pp. 361–367, doi: 10.1109/PESC.1982.7072429.

[8] C. Clark, A. Strain, and A. López-Mazarias, “A high performance, very low cost power system for microspacecraft,” in *Proc. 8th Eur. Space Power Conf.*, 2008.

[9] P. Rueda and B. Van der Weerdt, “Segregated maximum power point tracking based on step-up regulation,” in *Proc. 7th Eur. Space Power Conf.*, 2005.

[10] J. A. Carrasco, F. G. de Quirós, H. Alavés, and M. Navalón, “An analog maximum power point tracker with pulsewidth modulator multiplication for a solar array regulator,” *IEEE Trans. Power Electron.*, vol. 34, no. 9, pp. 8808–8815, Sep. 2019, doi: 10.1109/TPEL.2018.2886887.

[11] R. Leyva, C. Alonso, I. Queinnec, A. Cid-Pastor, D. Lagrange, and L. Martinez-Salamero, “MPPT of photovoltaic systems using extremum-seeking control,” *IEEE Trans. Aerosp. Electron. Syst.*, vol. 42, no. 1, pp. 249–258, Jan. 2006, doi: 10.1109/TAES.2006.1603420.

[12] D. Selcan, G. Kirbis, and I. Kramberger, “Analog maximum power point tracker for spacecraft within a low Earth orbit,” *IEEE Trans. Aerosp. Electron. Syst.*, vol. 52, no. 1, pp. 367–378, Feb. 2006, doi: 10.1109/TAES.2015.140279.

[13] E. Koutroulis and F. Blaajberg, “A new technique for tracking the global maximum power point of PV arrays operating under partial-shading conditions,” *IEEE J. Photovolt.*, vol. 2, no. 2, pp. 184–190, Apr. 2012, doi: 10.1109/JPHOTOV.2012.2183578.

[14] M. Miyatake, M. Veerachary, F. Toriumi, N. Fujii, and H. Ko, “Maximum power point tracking of photovoltaic arrays: A PSO approach,” *IEEE Trans. Aerosp. Electron. Syst.*, vol. 47, no. 1, pp. 367–380, Jan. 2011, doi: 10.1109/TAES.2011.5705681.

[15] K. S. Tey and S. Mekhilef, “Modified incremental conductance algorithm for photovoltaic system under partial shading conditions and load variation,” *IEEE Trans. Ind. Electron.*, vol. 61, no. 10, pp. 5384–5392, Oct. 2014, doi: 10.1109/TIE.2014.2304921.

[16] N. Femia, D. Granozio, G. Petrone, G. Spagnuolo, and M. Vitelli, “Predictive & adaptive MPPT perturb and observe method,” *IEEE Trans. Aerosp. Electron. Syst.*, vol. 43, no. 3, pp. 934–950, Jul. 2007, doi: 10.1109/TAES.2007.4383584.

[17] Y.-K. Chen, Y.-C. Lai, W.-C. Lu, and A. Lin, “Design and implementation of high reliability electrical power system for 2U NutSat,” *IEEE Trans. Aerosp. Electron. Syst.*, vol. 57, no. 1, pp. 614–622, Feb. 2021, doi: 10.1109/TAES.2020.3028488.

[18] M. Wirthlin, “High-reliability FPGA-based systems: Space, high-energy physics, and beyond,” *Proc. IEEE*, vol. 103, no. 3, pp. 379–389, Mar. 2015, doi: 10.1109/JPROC.2015.2404212.

[19] A. Garrigós, D. Marroquí, J. M. Blanes, R. Gutiérrez, M. Compadre, and C. Clark, “An analog global maximum power point tracking for photovoltaic systems: Application to nanospacecrafts,” in *Proc. 19th Eur. Conf. Power Electron. Appl.*, 2017, doi: 10.23919/EPE17ECCEEurope.2017.8098986.

[20] E. Turan, S. Speretta, and E. Gill, “Autonomous navigation for deep space small satellites: Scientific and technological advances,” *Acta Astronaut.*, vol. 193, pp. 56–74, 2022, doi: 10.1016/j.actaastro.2021.12.030.

[21] J. B. Pezent, R. Sood, A. Heaton, K. Miller, and L. Johnson, “Preliminary trajectory design for NASA’s solar cruiser: A technology demonstration mission,” *Acta Astronaut.*, vol. 183, pp. 134–140, 2021, doi: 10.1016/j.actaastro.2021.03.006.

[22] A. Capannolo et al., “Challenges in LICIA Cubesat trajectory design to support DART mission science,” *Acta Astronaut.*, vol. 182, pp. 208–218, 2021, doi: 10.1016/j.actaastro.2020.09.023.

[23] A. Edpuganti, V. Khadkikar, M. S. E. Moursi, H. Zeineldin, N. Al-Sayari, and K. Al Hosani, “A comprehensive review on CubeSat electrical power system architectures,” *IEEE Trans. Power Electron.*, vol. 37, no. 3, pp. 3161–3177, Mar. 2022, doi: 10.1109/TPEL.2021.3110002.

[24] J. A. Carrasco et al., “Micro-platform power system for scientific deep space exploration,” in *Proc. 12th Eur. Space Power Conf.*, 2019.

[25] A. Garrigós, J. L. Lizán, J. M. Blanes, and R. Gutiérrez, “Exploring the use of the LT3480 (RH3480) circuit as low-power, low-voltage solar array regulator,” in *Proc. 10th Eur. Space Power Conf.*, 2014.

[26] A. Fernandez, C. Baur, and F. Gómez-Carpintero, “Solar array hysteresis and its interaction with the MPPT system,” in *Proc. 10th Eur. Space Power Conf.*, 2014.

[27] AZUR SPACE Solar Power GmbH, Azurspace 3G30C Triple Junction Solar Cells-Datasheet, May 2019. [Online]. Available: http://www.azurspace.com/images/0003429-01-01_DB_3G30C-Advanced.pdf

[28] Saft Groupe SAS, SAFT MP174865xlr Rechargeable Li-Ion Cell-Datasheet, Apr. 2018. [Online]. Available: https://www.saftbatteries.com/products-solutions/products/mp-vl-batteries-launchers

[29] Electrical and electronic, ECSS-E-ST-20C Rev.2, Apr. 2022.

[30] EEE components, ECSS-Q-ST-30-11C Rev.2, Jun. 2021.

[31] C. Torres, J. M. Blanes, A. Garrigós, D. Marroquí, C. Orts, and J. A. Carrasco, “High-reliability solar array regulator proposal for harsh environments,” in *Proc. IEEE Mediterranean Electrotech. Conf.*, 2022, pp. 698–702.

Cristian Torres was born in Elche, Spain, in 1993. He received the B.Sc. degree in telecommunications technology engineering from the Miguel Hernández University of Elche, Elche, in 2019, and the M.Sc. degree in telecommunication engineering in 2020 from the Miguel Hernández University, Elche, where he is currently working toward the Ph.D. degree in industrial technologies.

In 2021, he worked as a Predoctoral Researcher with the Centre for Research on Microgrids, Aalborg University, Denmark . His main research interests include space power systems and industrial electronics.

Ausiàs Garrigós (Senior Member, IEEE) was born in Xixona, Spain, in 1976. He received the M.Sc. degree in electronic engineering from the University of Valencia, Valencia, Spain, in 2000, and the Ph.D. degree in space power electronics from Miguel Hernández University (UMH), Elche, Spain, in 2007.

He is currently a Professor with the Department of Electronics Technology, UMH. He was with CERN, Switzerland, from 2002 to 2004; ESA, The Netherlands, in 2008; and the University of Strathclyde, U.K., in 2015. He has participated in more than 30 research and technology transfer projects and coauthored around 90 international publications. Most of them are related to power electronics. His main research interests include space power electronics and their ancillary electronic systems.

José M. Blanes was born in Elche, Spain, in 1974. He received the M.Sc. degree in telecommunication engineering from the Universidad Politécnica de Valencia, València, Spain, in 1998, and the Ph.D. degree in industrial technologies from Miguel Hernández University, Elche, Spain, in 2011.

He is currently an Associate Professor with the Department of Materials Science, Optics and Electronics Technology, Miguel Hernández University. His main research interests include space power systems and industrial electronics.

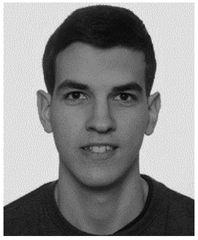

Pablo Casado was born in Monforte del Cid, Spain, in 1999. He received the B.Sc. degree in telecommunications technology engineering from the Miguel Hernández University of Elche, Elche, Spain, in 2021. He is currently working toward the M.Sc. degree in telecommunication engineering with Miguel Hernández University, Elche.

His main research interests include space power systems and industrial electronics.

David Marroquí was born in Elche, Spain, in 1990. He received the M.Sc. degree in industrial engineering from the Miguel Hernández University of Elche, Elche, Spain, in 2015, and the Ph.D. degree in industrial technologies from Miguel Hernández University, Elche, in 2020.

He is currently an Assistant Professor with the Department of Materials Science, Optics and Electronics Technology, Miguel Hernández University of Elche. He was Predoctoral Researcher with the Centre for Reliable Power Electronics, Aalborg University, Denmark, in 2018, and a Postdoctoral Researcher with the European Space Agency, Noordwijk, The Netherlands, during 2021–2022. His research interests include space power systems, industrial electronics, and electronics reliability.